5 Application of High Repetition Rate X-Rays in Diffraction Experiments

Besides the development of X-ray lasers and the use in micro-lithography the research on possible applications of radiation from laser, produced plasmas was driven by the opportunity to exploit their short wavelength as well as the short pulse length for structural investigation of matter. This idea is based on the fact that hard X-rays can couple directly with the core electrons which are localized spatially around the atomic nucleus and hence, sensitive to atomic arrangement. Many experiments towards such science have been made and are described in review articles (e.g. [KIE93], [VDL01], [ROU01]) and text books [HER97]. Most of the experiments focus on ultrafast changes in diffraction characteristics (e.g. [RRU97], [RRF01], [CRP99], [CWS99], [FEU01], [VDL01]). Only a few studies were done on ultra-fast chemistry (e.g. [RWJ96], [BKM01] using high harmonics). Time-resolved applications in biophysics are still restricted to synchrotron radiation [SRA96], although simulations show a great potential for intense ultrashort X-ray pulses [NWS00].
Most of the research done in the last decade in this field shows that, in contrast to synchrotron radiation, laser-plasma emission is still more the subject rather than a means of investigation. The work presented here has not the intention to change this completely but to present progress towards a more reliable and versatile setup for X-ray diffraction experiments. Using the X-ray source described in the previous chapter, Bragg diffraction experiments were conducted at 1 kHz repetition rate. Compared to other laser based X-ray sources (table 4-2), this means in particular to work with a low photon flux. In this chapter it will be shown that the photon budget of the gallium line radiation is fully sufficient for high-resolution diffraction experiments and hence, time-resolved experiments with a jet target are feasible.

5.1 X-Ray Detection Using a Back Illuminated CCD Camera

In Chapter 4 semiconductor diodes for X-ray detection have been presented. With the sophisticated electronics of the AMPTEK spectrometer this is sufficient for spectral measurements. But the resolution of such a system is limited to several hundred electron

volts. For experiments with higher energy resolution, other solutions are required. One is the use of a diffracting crystal and a spatially resolving detector. Using photographic plates this procedure has been known for almost a century. Today we can use charge-coupled devices (CCD) with their advantages of high sensitivity (down to single photon counting), digital signal output and rapid data processing capabilities.

5.1.1 CCD Types and Detection Principles

The fundamental function of such a CCD is not very different from the semiconductor devices described in Chapter 4. Actually one can understand such devices as one or two dimensional arrays of charge collecting detectors. The basic function is illustrated in Fig. 5-1. The detector consists of a silicon wafer (about 500µm thick) with a silicon oxide layer and an electrode structure on top. Impinging photons which are absorbed in the depletion layer and converted into photoelectrons will be detected by the electrode structure. This depletion layer is 10…20 µm thick. Photoelectrons from places deeper within the bulk silicon do not contribute.

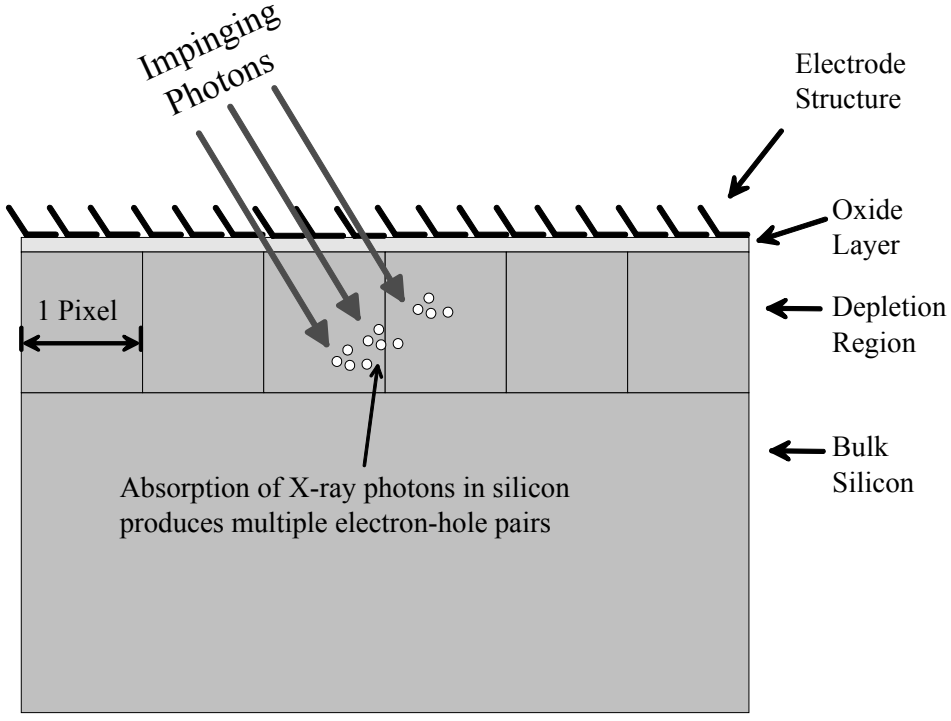

Fig. 5-1: Schematic illustration of the direct detection of X-ray photons [AND].

This is the detection principle of so called *front illuminated* CCD (FI). Their disadvantage is that most of the radiation is attenuated by the electrode structure on top of the detector. To overcome this problem several solutions have been developed. Fig. 5-2 shows a comparison of their detection efficiencies.

- Open electrode

  The electrode structure covers only half the pixel. This increases the quantum efficiency but the pixel capacity is reduced (saturation at half intensity)

- Back illuminated (or back thinned) (BN)

  In this case the whole structure is reversed: the photons impinge on the silicon and the electrode structure is on the backside. The silicon thickness is reduced to the size of the depletion region of about 20µm (therefore back thinned). The advantage of this structure is not only a higher quantum efficiency (Fig. 5-2), but also the possibility of coating the surface with filtering or protection layers.

- Deep depletion (DD)

  For deep depletion CCD a special silicon material with higher resistance and higher doping is used. Therefore the depletion region is thicker and the quantum efficiency is increased. The disadvantage of the DD devices is an increased noise (= dark current) level.

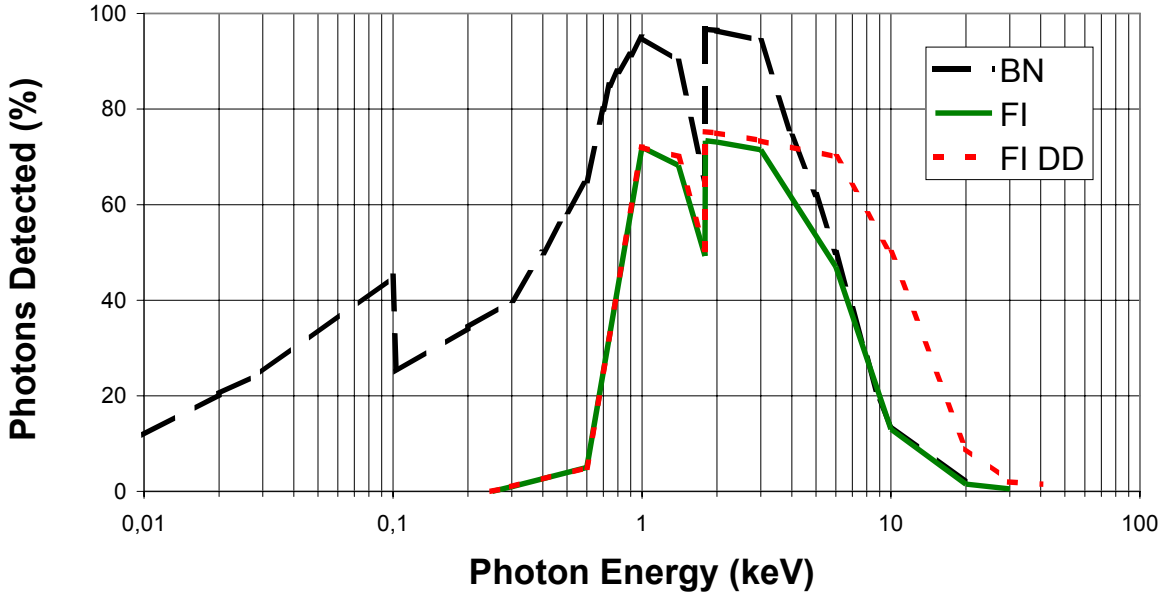

Fig. 5-2 : Quantum-efficiency curves for back illuminated (BN), front illuminated (FI) and front illuminated deep-depletion (FI DD) devices [AND].

From Fig. 5-2 it is apparent that for X-rays[1] with E > 6 keV the attenuation by the electrode structure is negligible compared to the decreased absorption cross section in silicon and hence, the difference between front illuminated and back illuminated devices vanishes. Deep-depletion CCD are sensitive up to higher photon energies because of their enlarged depletion region. For even harder X-rays the method of indirect detection should be considered. In this case the photons are detected by a phosphor or scintillator material and converted into visible light which, in turn, is detected by a CCD. The conversion material can be coated directly onto the CCD or onto a fiber optic array which transmits the visible light to a remote CCD.

5.1.2 X-Ray Detection with ANDOR DO434 BN

For the selection of an appropriate CCD according to a particular experiment, the quantum efficiency is a first criterion. A next question might be noise (particularly dark current). Table 5-1 shows the dark-current values depending on the detector temperature as specified by the manufacturer [AND] for the device used in the experiments described here. It is a back illuminated ANDOR DO 434 BN CCD with 1024×1024 pixel. It is specified that the BN model has about 2 times the dark current of a FI. The deep depletion CCD has about 1000 times higher dark current than the other two types [AND]. These figures differ due to particular devices and read-out settings. At low temperature the dark current should be negligible. However in some cases it might be necessary to work at room temperature. Cooling the detector to low temperature takes several 10 min which can be obstructing if the

Table 5-1: Dark current for ANDOR DO 434 BN CCD (Sr. No CCD – 2677).

Temperature [°C]	**Dark Current** [electrons/pixel × s]
0	4
-10	1
-20	0.3
-30	0.08
-40	0.02
-50	0.01

[1] A comparison for other spectral regions is given in the DO 434 specification [AND]. There the superior quantum efficiency of the BN over the FI type in NIR, visible and UV region is shown.

experimental time is limited (by the gallium jet running time), or the vacuum chamber has to be opened between experimental steps. For such a case the background noise for a back illuminated CCD (DO434 BN) was determined. With a stabilized detector temperature of 20°C, an average noise of 38.5 cts/s*pixel[1] was calculated for a 200 s test of the CCD without light exposure. This noise appears rather homogenously over the CCD; the standard deviation among the pixel values is only 0.6 % of mean value. Hence, the background can be removed by the background correction function almost perfectly. Using this built-in procedure of the camera software, the average noise was reduced to 0.17 cts/s*pixel. Further filtering techniques (Appendix B) can reduce the noise even more.

These noise numbers might be compared with the expected number of electrons created per X-ray photon. The number of photoelectrons N created in the CCD per photon depends on the photon energy E and the camera gain g : $N=E/g*3.65eV$. In the case of Gallium line radiation the photon energy of E=9.25 keV corresponds to about 1270 photoelectrons (gain g=2). Even with a quantum efficiency of 20%, this is still 250 counts per incident X-ray photon. With a noise level of 0.17 e/s*pix at 20 °C for the DO 434 BN, the rate of detected gallium line photons should then be greater than 0.0007 $(s*pixel)^{-1}$ or one photon per pixel in 1400 s.

The next criterion is the desired spatial resolution on the detector. The ANDOR DO 434 BN offers 13 µm × 13µm pixel size. This is almost the highest resolution available among nowadays X-ray CCDs. Larger pixels require a longer distance to the diffracting crystal for the same resolution and lead to a lower flux on the detector.

Summarizing one can see that the back illuminated CCD shows a signal-to-noise ratio 2 or3 orders better than the deep-depletion CCD while having only about half the quantum efficiency at 9 keV. Together with the superior pixel size, this decides the choice of the back-illuminated CCD ANDOR DO 434 BN with 1024×1024 pixels of 13µm size.

[1] averaged over column 800 to 1000 and all lines of the CCD

5.2 Experimental Setup

For the planning of a Bragg diffraction experiment, 3 points should be regarded first: (1) the matching of X-ray wavelength and crystal lattice constant, (2) appropriate setup dimensions and alignment precision for optimum resolution and (3) shielding for the reduction of noise due to diffracted laser light and scattered X-rays. The first point refers to the diffraction law for photons with wavelength λ on a crystal with the lattice constant d : $2d \sin\theta = m\lambda$. This implies the condition $\lambda < 2d$. Only photons with a wavelength smaller than two times the lattice constant can interfere and form a diffraction pattern. Table 5-2 shows the wavelength and the diffraction angles on a (111) surface of GaAs for radiation from water, copper and gallium targets. The last column in Table 5-2 shows the angular spread of the spin-orbit split components of K_α line radiation.

Table 5-2: Bragg diffraction constants for a GaAs (111) crystal surface (d=3.2639 Å) and the line radiation from water, copper and gallium (energy numbers from [XDB01]).

X-Ray Emission Line	Emission Energy [keV]	Wavelength [Ångstrom]	Bragg Angle θ (d=3.2639 Å) [Grad]	Angular Difference $d\theta = \theta_{\alpha1} - \theta_{\alpha2}$ [arcmin]
Water (O) $K_{\alpha1}$	0.5249	23.6	$\lambda >> 2d$	--
Cu $K_{\alpha1}$	8.04778	1.5406	13.651	--
Cu $K_{\alpha2}$	8.02783	1.5444	13.686	2.07
Ga $K_{\alpha1}$	9.25174	1.34013	11.847	--
Ga $K_{\alpha2}$	9.22482	1.34404	11.882	2.10

If the Bragg angle is determined, the geometrical dimensions can be considered. Assuming a distance of 600 mm between GaAs crystal and CCD one can calculate the spatial separation of the individual lines from their angular spread (assuming a point-like origin on the crystal). For the $K_{\alpha1}$ and the $K_{\alpha2}$ lines the difference angle is 2 arc min corresponding to 370 µm or 28 pixel separation on the CCD. The same estimation yields for the distance between $K_{\alpha1}$ and $K_{\beta1}$ about 980 pixel. This is a good compromise between resolution and intensity. Fig. 5-3 illustrates the experimental setup (for a detailed drawing see Appendix B.5). The tube between the vacuum chamber and the CCD is divided into a 300mm and a 100 mm piece so

that a reduction of the crystal-to-detector distance (for increased intensity) can easily be achieved.

To follow the optical path and alignment by using a pilot beam would be easy if crystal is cut perfectly. Unfortunately, the crystal cut is specified to +/- 0.5 deg precision only. This specification describes the angle between the optical surface (specular reflection) and the lattice planes (Bragg diffraction). That means that alignment using an HeNe-laser pilot beam on the reverse optical path is possible, but offers only the reduced precision. The open spatial angle of the CCD with respect to a point source on the crystal is about 1.2 deg. With an additional alignment error of about 1 deg, due to measurement errors, it is necessary to turn the crystal until diffraction lines appear on the CCD. If then a line pair appears it can be identified as K_α or K_β lines by their splitting ratio (Table 5-3).

Table 5-3: Relative intensities of gallium lines [XDB01].

Line	Energy [keV]	Relative intensity
Ga $K_{\alpha 1}$	9.2517	100
Ga $K_{\alpha 2}$	9.2248	51
Ga $K_{\beta 1}$	10.2642	66
Ga $K_{\beta 3}$	10.2603	5

Another important concern is the reduction of photonic noise. Scattered NIR and visible radiation from the laser plasma is blocked by a 30µm Al filter on the camera. This has to be fixed very carefully with an appropriate filter holder on the camera mount. The scattered X-rays have to be carefully blocked too. Three different lead plates with apertures of only a few mm are placed within the setup (Fig. 5-3 denoted by number 2…4) to accomplish this task.

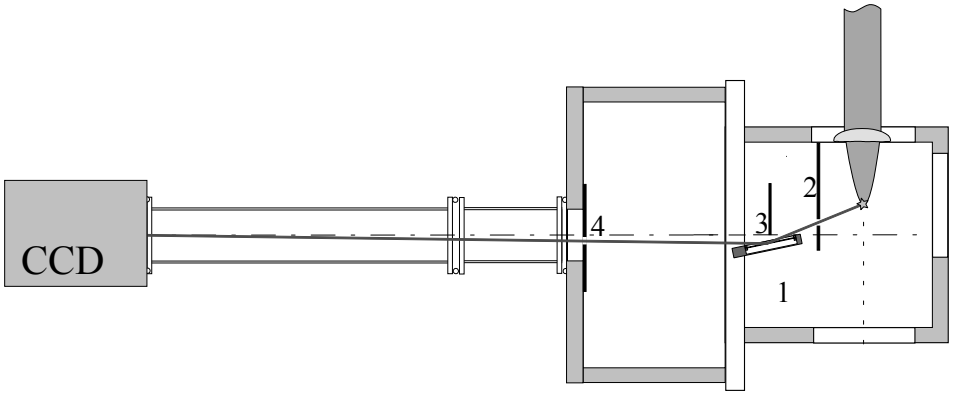

Fig. 5-3 : Scaled scheme (top view) of the experimental setup for Bragg diffraction using Ga K_α radiation from the laser produced plasma (1 GaAs diffraction crystal, 2…4 lead shielding).

Not shown in the setup scheme is the AMPTEK spectrometer. For simultaneous observation of the X-ray spectrum, it was mounted onto the vacuum chamber with 90 deg observation angle to jet and laser. All parameters of the spectrometer are similar to the setup described in Chapter 4.

Finally, one can estimate flux and contrast on the CCD. Taking the photon budget of 6×10^8 photons/s and a distance of about 0.7 m target-to-detector, the flux of Ga K_α photons per pixel (13x13µm²) is about 0.02 s^{-1}(assuming 100% transmission of the line radiation from the source to the CCD). With an experimental time of 200 s, this would lead to about 0.8 X-ray photons impinging on one pixel.

Using the estimation formula $N=E/g$*3.65 eV (gain g=2) for conversion of Ga K_α photons into photoelectrons (counts) and a quantum efficiency of 20%, the expected count rate per pixel is about 5 counts/s*pixel. Within 200s this should add up to about 1000 counts. Compared to the noise level of 0.17 cts/s*pixel the signal-to-noise ratio should be in the order of 30:1.

5.3 Diffraction on a GaAs Crystal

Diffraction can be used to investigate either the structure of the crystal or the nature of the applied radiation. In the experiments presented here, the crystal is known and some features of the apparatus and the radiation will be investigated. The crystal is a monolithic GaAs crystal as used in the semiconductor industry. It is cut parallel to the (111) plane. As most of the semiconductor materials, gallium arsenide has a zinc blende or ZnS lattice structure [KIT91]. Such crystals have a diamond structure consisting of two fcc (*face centered cubic*) lattices shifted by a quarter of the space diagonal. The gallium atoms are located on one fcc lattice and the arsenic atoms on the other one. The lattice parameter of an ideal GaAs crystal is 5.655360 Å with an standard error of 10 fm [GAS96].

5.3.1 Diffraction Theory

In the following some basic principles of diffraction experiments will be discussed. One can separate the approaches into a kinematic theory and a dynamic theory of diffraction [SHN00]. First some formulas of the kinematic theory will be given followed by a short introduction into the more complex dynamic diffraction theory.

In principle, one can treat diffraction on a crystal similar to the optical diffraction on a ruled grating: In both cases there is a periodic structure at which the incoming light is scattered. The phase difference between rays from adjacent scattering centres is similar and in both cases the contrast (delta or Airy distribution) depends on the number of illuminated lines (unit cells). Of cause, the scattering from the atoms and the electrons in the unit cell give a more complicated amplitude factor than the shape of the groves in the ruled grating.

As described in many text books on solid state physics (e.g. [WHS89], [KIT91], [WHA79]), the direction and amplitude of the scattered wave is derived starting with the electric field of a plane wave with frequency ω and a wave vector $\mathbf{k}=2\pi/\lambda$ incident on a multielectron atom:

$$E = E_0 \exp[i(\mathbf{kr} - \omega t)] . \qquad / \mathbf{5\text{-}1}$$

The atomic electrons re-emit X-rays in all directions:

$$E = \frac{E_0 f_d}{r} \exp[i\,(\mathbf{k'r} - \omega t)] \ . \qquad / \mathbf{5\text{-}2}$$

The electric field in /5-2/ is the solution of the wave equation where **k'** indicates the change in direction and phase of the wave vector, f_d denotes the *atomic scattering factor* of an atom indexed by a basis vector **d**. The atomic scattering factor f_d is defined as the ratio of the amplitude scattered by the actual electron distribution of the atom to the scattered amplitude of one isolated electron, and can be calculated using Hartree-Fock methods. Tabulated numbers for f_d and their limitations can be found at several places [FFDAT].

Now interference effects from waves diffracted from atoms at different places will be considered. In Fig. 5-4 a wave with wave vector **k** is scattered from an atom O at the origin and from an atom P separated by a lattice vector **R** and basis vector **d**. The phase difference between the scattered waves is $\Delta\mathbf{k}\,(\mathbf{R} + \mathbf{d})$ where $\Delta\mathbf{k} = \mathbf{k} - \mathbf{k'}$ is the *scattering vector*.

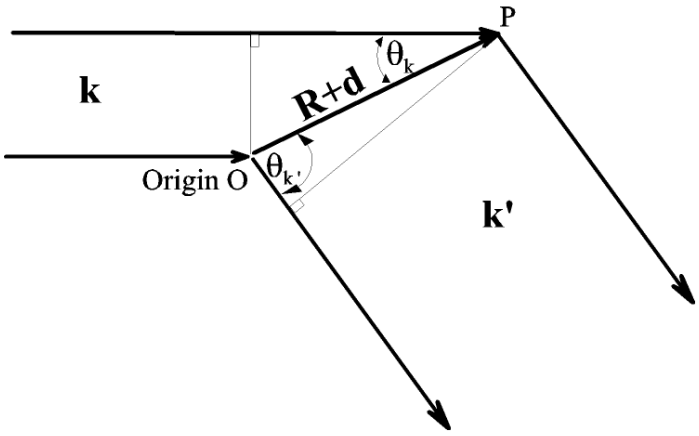

Fig. 5-4: Scheme of the phase difference between radiation scattered from an atom O at the origin and from an atom P at R + d.

The phase factor is then exp(0)=1 for the atom O and exp[i $\Delta\mathbf{k}(\mathbf{R}+\mathbf{d})$] for atom P. Summing the phase factors for all N unit cells (one dimensional) indexed by the lattice vectors **R,** and all atoms in the unit cell indexed by the basis vector **d**, one can define a *lattice structure factor* F_R:

$$F_R \equiv \sum_R \sum_d f_d \exp[i\Delta\mathbf{k}\,(\mathbf{R}+\mathbf{d})]\,. \qquad /\,5\text{-}3$$

This can be factorized into one sum over the lattice points **R** and one sum over atoms at **d** in a unit cell:

$$F_R \equiv \sum_R \exp[i\Delta\mathbf{k}\,\mathbf{R}] \sum_d f_d \exp[i\Delta\mathbf{k}\,\mathbf{d}]\,. \qquad /\,5\text{-}4$$

The first sum in /5-4/ describes the influence of the lattice while the second describes diffraction from the atoms of the basis (therefore it is defined as *basis structure factor*). In general, the first sum defines angle and contrast of the diffraction pattern and the second one relative amplitudes between reflexes from different crystal planes.

The diffraction angle θ for X-rays with wavelength λ is defined by the Bragg condition for constructive interference, which can be derived from the first sum in /5-4/, therein denotes *d* the spacing between adjacent {hkl} planes (h,k,l Miller indices), and *m* is an integer denoting the order of diffraction.

$$2d\sin\theta = m\lambda \text{ ´.} \qquad /\,5\text{-}5$$

Furthermore the lattice vector **R** can be set as **R** = n**a (**assuming a one dimensional lattice of N unit cells and a unit vector **a**) with n = 0,1,2…, N-1.That and the first term of the lattice structure factor can be calculated. The influence of this term on the diffracted intensity (therefore squared) is shown in /5-6/:

$$\frac{F_R^* F_R}{F_d^* F_d} = \frac{\sin^2 \frac{N\,\Delta\mathbf{k}\mathbf{a}}{2}}{\sin^2 \frac{\Delta\mathbf{k}\mathbf{a}}{2}}\,. \qquad /\,5\text{-}6$$

This is an expression for a delta distribution (similar optical diffraction phenomena on multiple slits [EH01]) and defines the contrast of the diffraction pattern.

The basis structure factor F_d expresses the sum of the diffracted waves from all atoms of a unit cell. Introducing the reciprocal space concept it can be shown that F_d depends only on the atomic scattering factor f_d , the coordinates of each atom j within the unit cell and the Miller indices of the diffracting planes[1]:

[1] Thermal dependencies, usually expressed by the Debye-Waller factor e^{-M_j}, are neglected for simplicity.

$$F_d(hkl) = \sum_j f_j \exp(hx_j + ky_j + lz_j)\,. \qquad / 5\text{-}7$$

Calculation of the basis structure factor shows that contributions from the atoms in a unit cell may cancel out completely (F_d = 0) and that the spot of the corresponding plane {hkl} is missing in the diffraction pattern.

The theoretical concept described so far can be used to calculate the angles and the relative intensities of the spots (or lines) in the diffraction pattern of a crystal. It is limited by the assumption that each X-ray photon scatters only once before it is detected. Furthermore a change of the wavelength when the X-ray wave is entering the material is neglected as well as absorption processes in the crystal. A more practical concern is the limitation apparent from formula /5-6/ to describe the acceptance angle (or diffracted line width) for a given X-ray wavelength.

These limitations can be overcome with a more complex approach, *the dynamic diffraction theory*. An introduction into this topic can be found in textbooks. (e.g. [ZAC45] or [SHN00]) In general terms the dynamic theory makes strict use of Maxwell's equations and distinguishes between waves inside and outside the crystal. The most popular approach (Ewald 1917 , M. von Laue 1931 [LAU31]) treats the wave propagation in a periodic medium as an eigenvalue problem and uses the boundary conditions to obtain Bragg reflected intensities. Of the many contributions to the method thereafter, only two should be mentioned here: Taupin developed the treatment of bent crystals [TAU64], and Takagi [TAK69] gave some special formulas for strained or distorted crystals. For future experiments, these two methods will play an important role because bent crystals will be necessary for an efficient transmission of X-rays onto diffraction substrates or for focussing of hard X-rays onto crystal surfaces (see e.g.[HWF98]). Takagi's formalism is important for experiments where the strain between crystal layers is measured with high temporal resolution ([CWS99], [VDL01], [CRP99] etc.).

For the experiments presented in this work the prediction of the acceptance angle of the GaAs crystal can be done using dynamical diffraction theory. Simple kinematic theory as shown in equation /5-6/ gives only a delta distribution for the diffracted amplitude. Fig. 5-5 shows the calculation of the reflectivity (so called "rocking curve") for monochromatic Ga $K_{\alpha 1}$ radiation (E= 9.2517 keV) on a thick GaAs crystal with (111) orientation using a dynamic diffraction calculation program[MIK96]. The result from dynamic theory for the acceptance angle of the GaAs crystal (17.2 arcsec FWHM) in Fig. 5-5 will be used for comparison with experimental data in the next section.

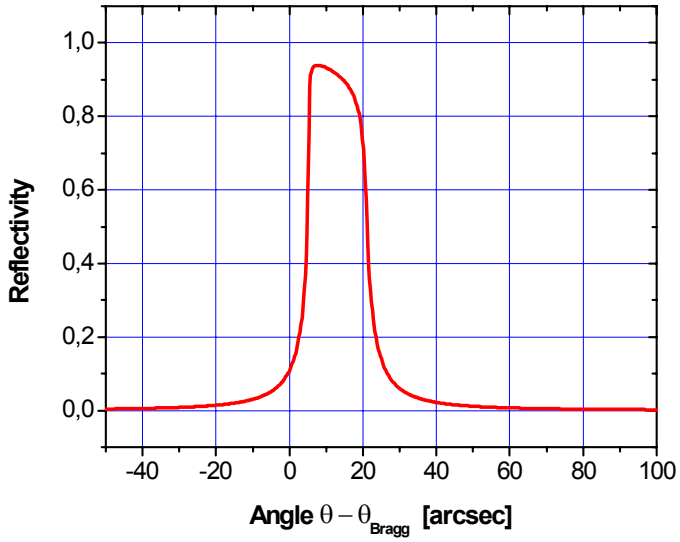

Fig. 5-5 : Simulated reflectivity ('rocking curve') based on dynamic diffraction theory for monochromatic Ga $K_{\alpha 1}$ line radiation diffracted on the (111) surface of a GaAs crystal. Calculation used XRDSL program (P. Mikulik [MIK96]).

5.3.2 Experimental Results

In the experiment with the setup described in section 5.2, a laser pulse of 3 mJ and 60 fs was used to create gallium K_α line radiation in a 30 µm gallium jet target. After appropriate alignment of the crystal, the diffraction pattern was recorded using the ANDOR DO 434 BN CCD camera. Fig. 5-6 shows the picture as received with the camera. To derive the full information from these pictures, data processing is necessary. This includes the following steps: background correction, band-pass filtering, camera tilt-angle correction, summarizing along the CCD columns, background offset subtraction and normalization. The full procedure of data processing is described in Appendix B. After data processing the lines in the picture can be identified by their intensity ratio of 1:2 as Ga K_α radiation (Table 5-3). The maximum amplitude of the diffracted lines in total numbers (Fig. B-1) is 6.36×10^5 counts in 200s per CCD-column) or 3.5 cts/s*pix. This is about 2/3 of the expected value of 5 cts/s*pix which can be explained with the splitting of the incident K_α radiation into 1/3 $K_{\alpha 2}$ and 2/3 $K_{\alpha 1}$.

The noise (standard deviation) after application of the different noise reduction methods (Appendix B) is reduced to 0.038 cts/s*pix or 1.1% of the peak value. This corresponds to a signal-to-noise ratio of about 100. This is comparable to results from copper targets [GUO97] with much higher laser pulse energy and higher Cu K_α flux (see table 4-2).

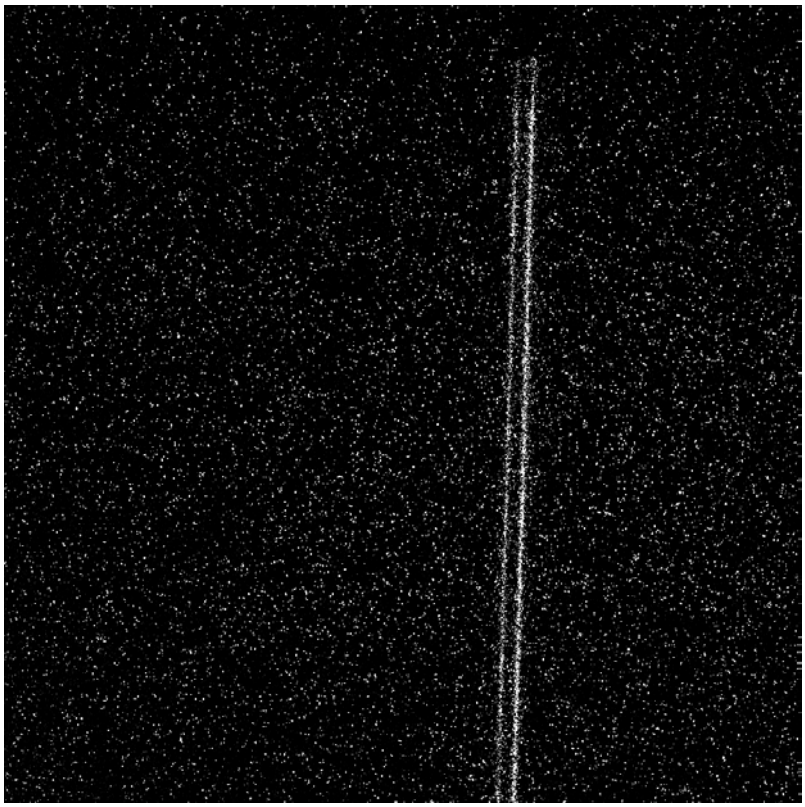

Fig. 5-6 : Gallium $K_{\alpha 1}$ and $K_{\alpha 2}$ line radiation diffracted on a GaAs crystal.

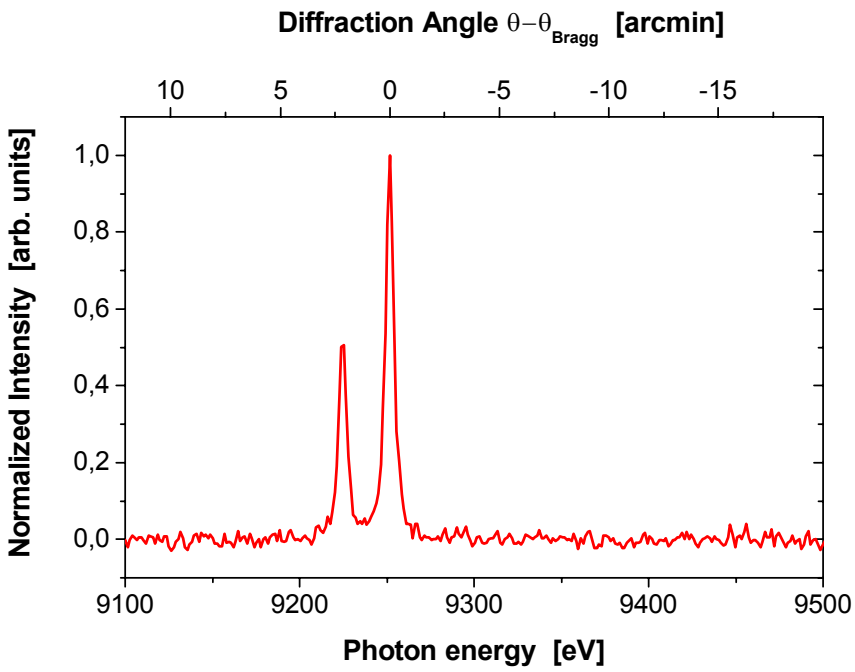

Fig. 5-7 : Calibrated intensity (reflectivity) of gallium lines after diffraction on a GaAs(111) crystal as derived from Fig. 5-6.

Once the lines are identified it is possible to calibrate the scale of the curve to angle or energy, according to the angular (energy) difference between $K_{\alpha 1}$ and $K_{\alpha 2}$ as calculated in Table 5-2. The calibrated diffraction curve of the two Ga K_α lines is shown in Fig. 5-7. If the resolution of the system is defined by one pixel, then the energetic resolution is 1.35 eV per pixel, although this might be enhanced using appropriate fitting techniques. The angular resolution is 0.1 arcmin/pixel or 6 arcsec/pixel. Using Gaussian fit functions the line width (FWHM) of the peaks in Fig. 5-7 is calculated to 28.0 ± 1.3 arcsec and 29.5 ± 1.2 arcsec for $K_{\alpha 2}$ and $K_{\alpha 1}$, respectively. The error bars in this calculation are deduced from the deviations of the experimental data from the fit curve (standard deviation of the width fit parameter).

The detailed results for energy width and angular width are given in Table 5-4. The simulation for the reflectivity of the crystal ('rocking curve') for monochromatic Ga $K_{\alpha 1}$ radiation (see Fig. 5-5) resulted in a peak width (FWHM) of 17.2 arcsec for the reflection on a GaAs (111) surface. This corresponds to about 3 pixels or 3.9 eV in the local calibration in the CCD camera plane. This simulation has been done for monochromatic radiation of negligible line width. For a comparison with the experimental data (in zero order), the natural line width of Ga $K_{\alpha 1}$ of 2.59 eV or 11.5 arcsec in the local calibration (FWHM, 6% error, [KO79]) should be added. This results in a comparison for the width (FWHM) of the diffraction curve of Ga $K_{\alpha 1}$ radiation on a (111) GaAs surface:

- Theoretical prediction: 28.7 ± 0.7 arcsec
- Experimental line width 29.5 ± 1.2 arcsec

This is a very good agreement between theoretical prediction and experimental data. It shows the high precision of the experimental method as well as the high quality of the GaAs crystal used in the experiment. A similar agreement was found with 10 Hz laser systems [GUO97].

Table 5-4: Energetic and angular width of the GaAs diffraction curve calculated from the calibrated data in Fig. 5-7 using a Gaussian fitting curve.

Line Radiation	Absolute energy [XDB01] [eV]	Angular width (FWHM) [arcsec]	Energetic width (FWHM) [eV]	Natural line width [KO79] (FWHM) [eV]
Ga $K_{\alpha 1}$	9 251.7	29.47 ± 1.15	6.63 ± 0.26	2.59 ± 0.69
Ga $K_{\alpha 2}$	9 224.8	28.01 ± 1.31	6.30 ± 0.29	2.66 ± 0.71